PHYSICAL REVIEW FLUIDS **1**, 074202 (2016)

Wettability controls slow immiscible displacement through local interfacial instabilities

Michael Jung, Martin Brinkmann,* and Ralf Seemann
Max Planck Institute for Dynamics and Self-Organization, 37077 Göttingen, Germany
and Experimental Physics, Saarland University, 66123 Saarbrücken, Germany

Thomas Hiller
Max Planck Institute for Dynamics and Self-Organization, 37077 Göttingen, Germany
and Institute for Applied Geophysics and Geothermal Energy, RWTH Aachen, 52074 Aachen, Germany

Marta Sanchez de La Lama
Max Planck Institute for Dynamics and Self-Organization, 37077 Göttingen, Germany
and Department of Geosciences, University of Oslo, 0315 Oslo, Norway

Stephan Herminghaus
Max Planck Institute for Dynamics and Self-Organization, 37077 Göttingen, Germany
(Received 17 May 2016; published 3 November 2016)

Immiscible fluid displacement with average front velocities in the capillary-dominated regime is studied in a transparent Hele-Shaw cell with cylindrical posts. Employing various combinations of fluids and wall materials allows us to cover a range of advancing contact angles $46^\circ \leqslant \theta_a \leqslant 180^\circ$ of the invading fluid in our experiments. In parallel, we study the displacement process in particle-based simulations that account for wall wettability. Considering the same arrangement of posts in experiments and simulation, we find a consistent crossover between stable interfacial displacement at $\theta_a \lesssim 80^\circ$ and capillary fingering at high contact angles $\theta_a \gtrsim 120^\circ$. The position of the crossover is quantified through the evolution of the interface length and the final saturation of the displaced fluid. A statistical analysis of the local displacement processes demonstrates that the shape evolution of the fluid front is governed by local instabilities as proposed by Cieplak and Robbins for a quasistatic interfacial displacement [Cieplak and Robbins, Phys. Rev. Lett. **60**, 2042 (1988)]. The regime of stable front advances coincides with a corresponding region of contact angles where cooperative interfacial instabilities prevail. Capillary fingering, however, is observed only for large θ_a, where noncooperative instabilities dominate the invasion process.

DOI: 10.1103/PhysRevFluids.1.074202

I. INTRODUCTION

Flows of immiscible fluids through a porous matrix are involved in many industrial and technological applications, for example, fuel cells [1–3], secondary oil recovery, and ground water flow [4–7]. Pressure-driven fluid displacement has been studied experimentally in flat beds of spherical particles [8–11], various model sandstones [12–14], and effectively two-dimensional microfluidic networks [15–18]. Despite these enormous activities to experimentally monitor and model immiscible flows in porous media, many details of the displacement process on the pore scale and their implications on the overall dynamics of the invading front remained unclear [19,20]. Only recently, the competition between wetting forces and viscous stresses on the pore scale has been investigated in experiments [11] and two-dimensional simulations [21], but the coherent description

---

[*] martin.brinkmann@physik.uni-saarland.de

of immiscible fluid displacement from pore scale to sample scale at various wetting conditions is still lacking. This applies, in particular, to the industrially relevant case of small average velocities of the invading front [7]. Open questions concern the interplay of wettability, geometry, and disorder of the porous matrix in the displacement process [2,10,21–27], as well as the role of inertia during local interfacial instabilities at the progressing front [28–31].

Several fundamental aspects of immiscible two-phase flow in porous solids have been studied in effectively two-dimensional model systems [15–17,21–23,32–34]. In a pioneering experimental work, Lenormand *et al.* [15] and later Zhang *et al.* [16] monitored local displacement processes in flat and transparent micromodels of two-dimensional channel networks that allowed real-time imaging of the advancing interfaces by optical microscopy. According to these works, the displacement of a wetting by a nonwetting fluid can be grouped into different regimes according to the global capillary number $\mathrm{Ca} \equiv U\mu_i/\gamma$ and the viscosity ratio $\mathsf{M} = \mu_i/\mu_d$ of the invading (i) and defending (d) fluid [15,16]. Here U denotes the average front velocity and γ the interfacial tension of the fluid-fluid interface, while μ_i and μ_d are the dynamic viscosities of the respective fluids. For sufficiently small capillary numbers $\mathrm{Ca} \ll 1$, the entire displacement process is dominated by interfacial forces and is largely insensitive with respect to the average displacement velocity U and fluid viscosities μ_i and μ_d.

In the limit of slow invasion, the evolution of the interface can be regarded as quasistatic for most of the time. Periods of gradual changes of the meniscus geometry are interrupted by sequences of fast instabilities of the fluid interface. For the case of invading fluids forming a high contact angle with the walls (drainage), the condition that a meniscus undergoes an instability and advances into an empty pore is independent on the configuration of neighboring menisci [15,32]. For the case of small contact angles (imbibition), however, the instabilities leading to interfacial advance are governed by the state of two or more adjacent menisci bounding the same pore [32,35]. The proposed cooperative nature of the latter type of instabilities manifests in a largely reduced roughening of the invading interface and is also identified as one of the main causes of a low residual saturation of the defending fluid.

A numerical model to describe slow quasistatic fluid invasion into a porous matrix for different wetting conditions was proposed by Cieplak and Robbins [22,23]. Arrays of circular disks with randomized radii but centered on a triangular or square lattice serve as model porous media with regular pore geometry. Front progression is described by a sequence of mechanically stable meniscus configurations attained during the slow rise of the driving pressure difference P between the invading and the defending fluid. Configurations of individual menisci are governed by the magnitude of P that fixes the in-plane radius $r \propto P/\gamma$ of all menisci being part of the invading front. As the pressure difference P increases, these menisci are subject to certain types of cooperative and noncooperative interfacial instabilities that trigger sudden local advancements of the front [22–24]. Both types of instabilities are controlled, besides the Laplace pressure P, by the local disk configuration and contact angle θ. The crossover between compact displacement patterns for imbibition and capillary fingering observed for drainage is explained through a competition between different types of interfacial instabilities [22–24]. Conclusions about the fluid dynamics of the rearrangements following these instabilities as well as the new stable configuration attained after the instability cannot be reached within the model of Cieplak and Robbins.

The aim of the present article is twofold. First, we want to explore whether the mechanisms put forward by Cieplak and Robbins hold true in a "real system" that is quasi-two-dimensional but exhibits the full fluid dynamics. This is studied both in experiments and in simulations. Second, we investigate whether the reported transition occurs as well in other types of randomness. While Cieplak and Robbins studied arrangements of circular obstacles with randomized radii but centered on regular lattices, we investigate the effect of positional randomness. To this end, we consider immiscible two-phase flow in a transparent microfluidic Hele-Shaw cell that is decorated with cylindrical posts of uniform diameter [see Fig. 1(a)]. Using different device materials and combinations of defending and invading fluids in our experiments, the advancing contact angle θ_a of the invading fluid is systematically varied from about 46° to about 180°. Displacement patterns for contact angles lower than 46° showed a strong dependence on the global shape of the Hele-Shaw cell and are thus discarded

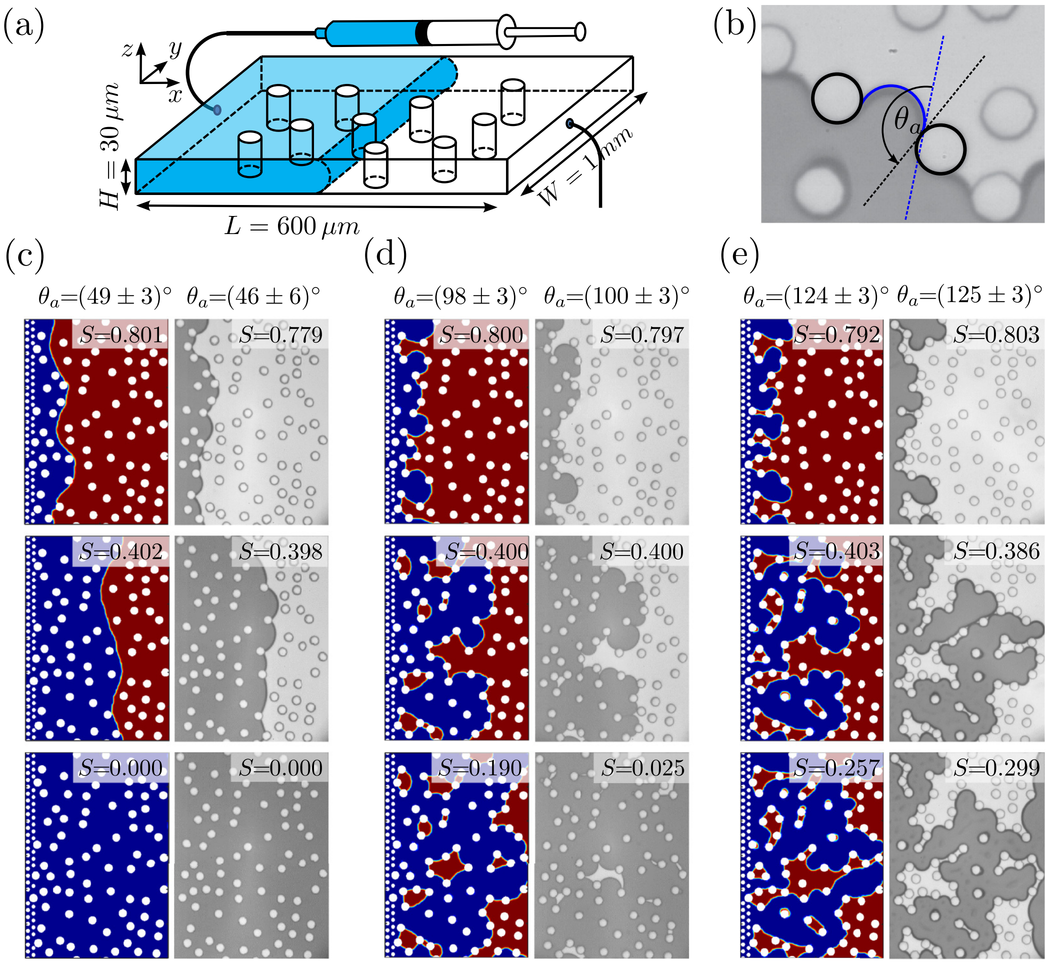

FIG. 1. (a) Sketch of the Hele-Shaw cell with cylindrical posts employed in our experiments. The experimentally captured area has a width of $W^* = 800\ \mu$m and an extension of $L^* = 600\ \mu$m. (b) Definition of the advancing contact angle θ_a with respect to the invading fluid. (c)–(e) Time series showing the evolution of the displacement pattern for different contact angles θ_a with an area fraction of posts $\phi = 0.15$ in simulations (left rows) and experiments (right rows). The invading fluid is injected from the left, with a similar velocity in all experiments shown here. Images are labeled with the respective saturations S of the displaced fluid.

from further analyses. Our fluid dynamics simulations, however, cover the full range of contact angles from complete wetting ($\theta_a = 0°$) to completely nonwetting ($\theta_a = 180°$) invading fluids.

Figures 1(c)–1(e) display examples of three generic displacement patterns, as found in our experiments and fluid dynamics simulations for different wetting conditions of the invading fluid. A comparison of the snapshots of fluid distributions between the wetting and the nonwetting invading fluids nicely illustrates the pivotal role of wettability during interfacial advance. To facilitate a comparison of the evolving fronts, we labeled the snapshots with the corresponding fraction $S \equiv V_d/V^*$ of the volume of the displaced fluid in the field of view V_d relative to the available cell volume V^*. For a small advancing contact angle $\theta_a \lesssim 80°$, as shown in the example Fig. 1(c), the invading front remains smooth and is able to completely sweep out the defending fluid. At intermediate advancing contact angles $80° \lesssim \theta_a \lesssim 120°$, including the example in Fig. 1(d), the front slightly roughens and leaves behind minute amounts of the defending fluid. Here the invading fluid already bypasses some regions of increased post density and thus traps small pockets of the defending fluid. For the case of a large contact angle $\theta_a \gtrsim 120^\circ$ as shown in the examples Fig. 1(e), we observe ramified displacement patterns, in full agreement with the predictions of Lenormand [15]. Long fingers of the invading fluid that reconnect to the fluid interface occasionally create large loops. Because this reconnection occurs in an effectively two-dimensional Hele-Shaw geometry, a substantial amount of the defending fluid disconnects from the upstream fluid reservoir and consequently remains trapped between the posts [see Fig. 1(e)]. The spectrum of displacement patterns for different wettability shown in Figs. 1(c)–1(e) is a consequence of local interfacial instabilities at the front, which govern the dynamics of the invasion process.

Results of both our experiments and full-scale fluid dynamic simulations corroborate that the slow interfacial displacement in our model Hele-Shaw cell is indeed controlled by wettability: The contact angle of the invading fluid with the wall selects which class of interfacial instability dominates the local interfacial advance. As we are going to demonstrate in this work, the relative frequencies of these advancing modes are highly sensitive with respect to changes in the wall wettability.

Before presenting the results, we will proceed with a short description of our experimental setup and protocols in Sec. II and give a brief outline of the method underlying our fluid dynamic simulations in Sec. III. To capture the different aspects of the displacement processes for small and large contact angles and to compare the front evolution with the one predicted by the model of Cieplak and Robbins, we quantify the evolution of the fluid distribution through the length of the fluid interface (see Sec. IV A). In Sec. IV B we introduce the different classes of local advancing modes, while in Sec. IV C we discuss the clear correlation between the dominant instabilities observed and the morphology of the final displacement pattern. We summarize our findings and give an outlook for future research in Sec. VI.

II. EXPERIMENT

Microfluidic Hele-Shaw cells of a width $W = 1000\ \mu\text{m}$ and height $H = 30\ \mu\text{m}$ equipped with randomly placed nonoverlapping cylindrical posts of radius $R = 16\ \mu\text{m}$ are fabricated by soft-lithographic methods [36] [see Fig. 1(a) and also Fig. 8 in Appendix A]. In our experiments we consider disordered post arrays with area fractions $\phi = 0.15$ and 0.3, corresponding to an average surface-to-surface separation between two neighboring posts of $\langle D\rangle = (43 \pm 22)\ \mu\text{m}$ and $\langle D\rangle = (27 \pm 13)\ \mu\text{m}$, respectively (corresponding to $\langle D\rangle \approx 1.4H$ for the dense and $\langle D\rangle \approx 0.9H$ for the dilute post configuration). For manufacturing reasons, the minimum value of D is set to the radius $R = 16\ \mu\text{m}$ for both structures. Typical for the lithographic fabrication process, we find a roughness of the sidewalls of the posts and the microfluidic cell on the order of a few hundred nanometers, but well below a micrometer. To reduce the influence of undesired boundary effects at the sidewalls of the cell we enlarge the imaged area of the cell by two rows of posts to each side. The field of view in our experiments has a width of $W^* = 800\ \mu\text{m}$ and extends over a length of $L^* = 600\ \mu\text{m}$ into the downstream channel direction. As device material we use oil resistant UV-curable adhesives NOA 83H or NOA 61 (Norland optical adhesives). The adhesives are molded from Sylgard 184 (Dow Corning) masters, which were previously molded from photolithographically fabricated SU-8 structures (Microchem. Corp.). The adhesive replicas of the device master are bonded to glass microscopy slides and connected to Teflon tubing. Microfluidic devices fabricated in this way are connected to either a computer-controlled syringe pump for a controlled volume flux or a hydrostatic reservoir for a pressure-controlled flow. In the range of the considered front velocities, the viscous pressure drop in the tubing is smaller than 1% of the pressure drop inside the microfluidic device and can thus be safely neglected. Whenever air is the invading fluid we take care that the displacement velocity is sufficiently slow so that compressibility effects can be neglected. Because of the compliance of the injected gas phase, the latter experiments operate in the pressure-controlled case for high front velocities. However, a direct influence of compressibility on the flow pattern at the front can be safely neglected as the Mach number is $\text{Ma} < 10^{-6}$ for all experiments.

The wetting conditions are varied by combining different device materials, invading, and defending fluids. In this way, we are able to cover a range of advancing contact angles $0^\circ < \theta_a \leqslant 180^\circ$ in our experiments. A summary of the respective material parameters is given in Table I of Appendix A. For each combination of invading and defending fluid, we measure the interfacial tension γ with the pendant drop method, while the advancing contact angle θ_a and the receding contact angle θ_r with respect to the invading fluid are determined with an optical contact angle measurement device (OCA 20, dataphysics) on flat samples of the corresponding material. The results of the measurements are summarized in Table II of Appendix A. As long as all menisci of the front are only advancing, there will be no impact of the receding contact angle on the evolution of the front morphology. Thus, we will exclusively refer to the advancing contact angle θ_a in the following.

Combinations of fluids with a too small value of the contact angle $\theta_a \lesssim 45^\circ$ are discarded from our experimental analysis. In this range of low contact angles the invading fluid preferentially spreads along the edges of the cell formed by the vertical sidewalls and the bottom or ceiling [37], leading to an undesired globally concave front morphology and parasitic instabilities.

Prior to a displacement experiment the microfluidic device is completely filled with the defending fluid. Subsequently, the invading fluid is injected while the displacement pattern is imaged at up to 500 frames per second with a high-speed camera (Photron SA3) mounted to an inverted microscope (Reichert-Jung MeF3) in transmission mode. The experiment is stopped once a stable fraction of the defending fluid is reached. All recorded images are first smoothed with an anisotropic diffusion filter at default settings using the freely available software IMAGEJ. After smoothing, the configuration of the invading front is analyzed with Image Pro Plus (version 6.3, Media Cybernetics). To this end, an image of the post array taken before fluid invasion is subtracted from all images. Subsequent thresholding is employed to identify the cell regions that are occupied by the injected fluid. To estimate the saturation S of the defending fluid in our experiments and simulations, we divide the area occupied by the defending fluid by the total available area of the field of view, respectively, of the simulation box. Because the finite horizontal extension of the meniscus for a contact angle $\theta_a \neq 90^\circ$ that scales linearly with the height H of the Hele-Shaw cell, we can expect a small systematic error in our estimate of S. In the present study, this error is less than 1% and hence much smaller than the statistical error of the average saturation taken over different experimental realizations.

III. NUMERICAL MODEL

Numerical simulation of immiscible fluid displacement in Hele-Shaw cells with cylindrical posts arranged in the same geometry as in the experiments described above are carried out with a multicolor stochastic rotation dynamics (SRD$^{\mathrm{mc}}$) algorithm [38–40]. Similar to the majority of off-lattice particle-based simulation methods, including the standard SRD algorithm for single phase fluids [41,42], the present algorithm provides an effective scheme to exchange linear momentum between fluid particles. The dynamics of the particles consists of a sequence of streaming and collision steps. During streaming, particles move deterministically between time t and $t + \Delta t$,

$$\mathbf{x}_i(t + \Delta t) = \mathbf{x}_i(t) + \mathbf{v}_i(t)\Delta t, \tag{1}$$

with $\mathbf{x}_i$ and $\mathbf{v}_i$, the corresponding position and velocity of particle i, respectively. In order to exchange linear momentum, the particles are sorted into cubic collision cells of side length a where the number of particles per cell fluctuates around an average value $\langle N \rangle$. The particle velocities $\mathbf{v}_i(t + \Delta t)$ after the collision are related to the precollisional velocities $\mathbf{v}_i'(t + \Delta t)$ through

$$\mathbf{v}_i(t + \Delta t) = \mathbf{u}(t + \Delta t) + \boldsymbol{\Omega}\{\mathbf{v}_i'(t + \Delta t) - \mathbf{u}(t + \Delta t)\}, \tag{2}$$

where $\mathbf{u}$ is the center-of-mass velocity of fluid particles in the corresponding collision cell and $\boldsymbol{\Omega}$ denotes the collision operator. The collision operator locally conserves linear momentum and mass which implies that averaged quantities such as density and flow velocity obey macroscopic transport equations. Additionally, to conserve locally the kinetic energy inside a collision cell we apply a cell level thermostat as described in Ref. [40]. For an extensive overview on the SRD method the reader is referred to [43,44].

Numerically efficient nonlocal collisions render the multiparticle simulation approach particularly suited for applications where details of interactions between fluid particles are largely irrelevant. Compared to molecular dynamics (MD) and dissipative particle dynamics [45–47] simulations, particle-based simulation methods like SRD require significantly less time averaging, or coarser time steps, to obtain reliable estimates of fluid motion in the continuum limit.

To simulate the flow of two immiscible fluids in our displacement experiments we adapt the ($\mathrm{SRD}^{\mathrm{mc}}$) collision operator of Inoue *et al.* [38] that actively drives a segregation between fluid particles with different *colors* (i.e., species). For the particular purpose of the present work, we extend Inoue's ($\mathrm{SRD}^{\mathrm{mc}}$) algorithm to account for different relative adhesion of the fluids to the walls of the flow cell. The distribution of local capillary and viscous stresses in the fluids is directly obtained from averages of the momentum flux over a dense mesh of small control planes. For details of the simulation method and our implementation of wall wettability, we refer the reader to Ref. [40].

To simulate forced fluid displacement from a quasi-two-dimensional Hele-Shaw cell with cylindrical posts, we set up a flat simulation box of length $L = 200\,a$, width $W = 150\,a$, and height $H = 3\,a$. Flat cylindrical posts with in-plane centers coordinates (x,y) are placed in the interval $[55\,a, 155\,a] \times [0, W]$ and the radius of the posts is set to $R = 3\,a$. The positions of post centers, however, are chosen to be identical to those in the Hele-Shaw cell used in our experiments. Periodic boundary conditions are applied into the vertical z direction to eliminate the constant offset of the pressure difference between the two fluids caused by the out-of-plane curvature of the meniscus. A no-slip boundary condition is enforced on the sidewall of the posts.

The pressure difference P between the invading and the displaced fluid is created in a narrow stripe between $x = 0$ and $x = 40\,a$ upstream of the cylindrical posts through a constant force f on the fluid particles into flow direction. Fluid particles that leave the simulation box at the downstream end $x = L$ experience an acceleration in the x direction entering the box from the upstream side at $x = 0$. A dense row of posts with a small radius $R = 0.5H$ and surface-to-surface distance $\langle D\rangle \approx 0.57H$ placed behind the inflow region acts as a barrier for the nonwetting fluid. The pressure difference P driving the invasion is now controlled through the magnitude of the force f, which is slowly ramped up in time. In order to remain close to a quasistatic situation, the force is incremented by a small step only after the averaged flow rate of the displaced fluid has fallen below the threshold value. This value was determined by the average flux out of the domain at $x = L$ at thermal equilibrium without driving. In all particle-based methods a pressure difference amounts to a difference in bulk densities between the fluids. For the particular protocol, this density difference across the whole region of interest is always smaller than 15% and does not affect the local interfacial tension and bulk viscosities of the fluids [40].

IV. RESULTS

The influence of wettability on the displacement of immiscible fluids becomes apparent in particular for small interface velocities where capillary stresses dominate over viscous stresses. The typical magnitude of the ratio of viscous stresses to capillary stresses is expressed by the dimensionless capillary number. In our experiments, the average velocity of the front varies from $U = 8 \times 10^{-5}$ to 4.3 mm/s, which corresponds to capillary numbers $\mathrm{Ca} = \eta U/\gamma$ ranging from 2.8×10^{-9} to 1.5×10^{-4}, respectively. The capillary number in our simulations is found between 8×10^{-3} and 2×10^{-2}, i.e., the values are systematically higher than in our experiments. Values of a modified capillary number Ca^* that accounts for the cell geometry [17] are always below $\mathrm{Ca}^* \approx O(1)$ in our experiments. In our simulations, however, this modified capillary number reaches $\mathrm{Ca}^* \approx O(10)$ and viscous effects may come into play during displacement. Nonetheless, a noticeable influence of the fluid viscosities on the distribution of the defending fluid is observed neither in experiments nor in numerical simulations up to the respective maximum velocities. Numerical values of the modified capillary number Ca^* corresponding to our experiments and simulations are given in Appendix B.

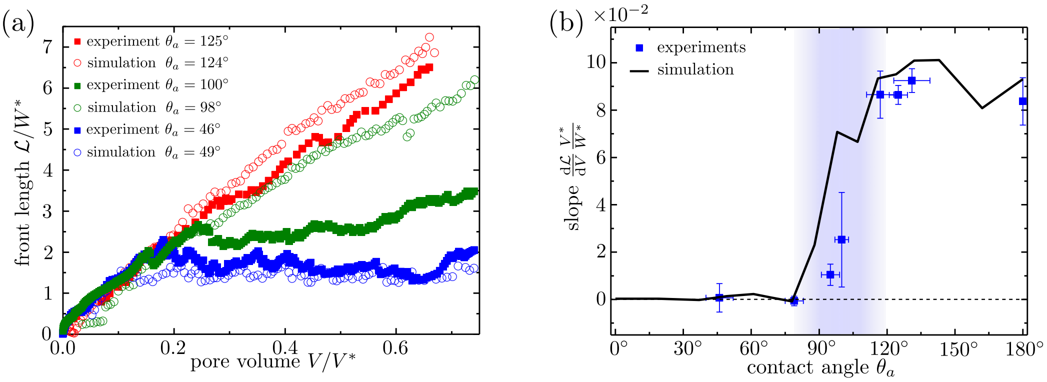

FIG. 2. (a) Evolution of the interfacial length $\mathcal{L}$ in units of the width W^* of the field of view for different advancing contact angles θ_a as a function of the injected volume V in units of the volume V^* of the captured area. (b) Fitted slope of the curves in (a) in the range $0.2 \leqslant V/V^* \leqslant 0.6$ as a function of the contact angle θ_a. Error bars of θ_a represent the standard deviation of several measurements, whereas the error bars of the slope $(V^*/W^*)(d\mathcal{L}/dV)$ represent the error of the fit. The shaded area highlights the crossover from stable interfacial advance to capillary fingering.

A. Displacement pattern

The crossover between stable interfacial advance and the formation of ramified fluid morphologies is apparent from the snapshots shown in Fig. 1. To reach a quantitative analysis of the displacement patterns of the invading fluid, we have to identify suitable order parameters that are sensitive to this crossover. A clear distinction between stable and ramified displacement patterns can be based on the temporal evolution of the total length $\mathcal{L}$ of the fluid-fluid interface, where we include the interface of entrapped pockets of the defending fluid. For a stable interfacial advance, the interface length $\mathcal{L}$ fluctuates around a constant value being close to the width W^* of the field of view. In the case of a branched displacement pattern, i.e., at high contact angles of the invading fluid, the total length of the interface should increase with time t at a rate $d\mathcal{L}/dt > 0$.

Figure 2(a) exemplifies the evolution of the interface length $\mathcal{L}$ in units of the width W^* for three contact angles that are representative for a wetting, an intermediate, and a nonwetting condition. Because the injection rates for various experimental realizations and simulations differ, the rescaled length $\mathcal{L}/W^*$ in Fig. 2(a) is plotted as a function of the injected volume V normalized by the total volume V^* (see Sec. II). During an initial phase $V \lesssim 0.2V^*$, we observe the buildup of an invading front at the upstream side of the field of view. Only the data for $V \gtrsim 0.2V^*$ are specific for the contact angle θ_a and further analyzed. For contact angles $\theta_a \lesssim 80°$, the interface length $\mathcal{L}$ as a function of V/V^* displays a plateau in both experiments and simulations. For contact angles $\theta_a \gtrsim 80°$, the interface length increases almost linearly with the fraction of the injected volume V/V^*. The corresponding average slope $d\mathcal{L}/dV$ increases as the contact angle becomes larger. To quantify the increase of the normalized interfacial length $\mathcal{L}/W^*$ with V/V^*, we fit the data in the range of injected volume $0.2 \leqslant V/V^* \leqslant 0.6$ with a linear relation. Within this range of volumes, the interface of the invading fluid has not yet left the field of view at the downstream end. In contrast to the experimental data, we observe a slightly sublinear growth of $\mathcal{L}$ with V in our numerical data.

Figure 2(b) displays the magnitude of the slope plotted against the contact angle θ_a. The onset of a progressive lengthening of the front during invasion can be located at $\theta_a \approx 80°$. At high contact angles $\theta_a \gtrsim 120°$, however, the slope saturates to a constant value. Changes in the growth of interfacial length and the corresponding front morphology also imply changes in the saturation of the defending phase that remains in the cell after fluid invasion. Figure 3(a) provides examples of the general form of the saturation S of the defending fluid as a function of the injected volume V/V^* for different contact angles θ_a. Because the volume of the incompressible fluids is conserved, the

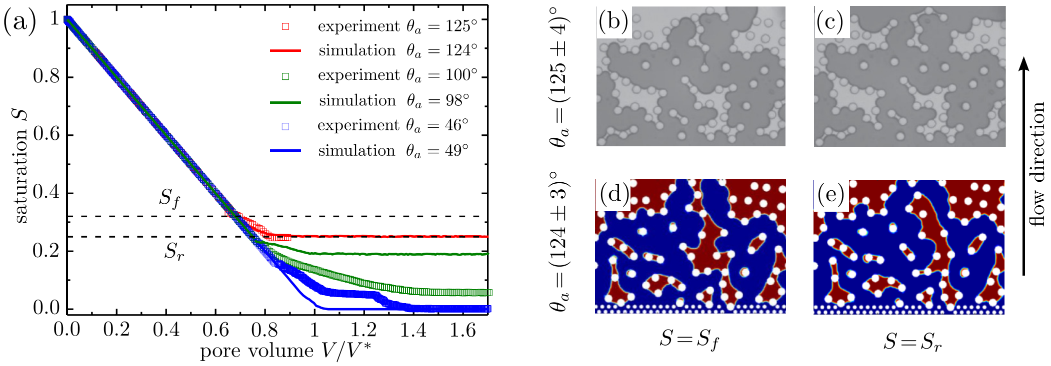

FIG. 3. (a) Saturation S_d of the defending fluid as a function of the pore volume V/V^* of the invading fluid. A first kink at $S = S_f$ corresponds to the breakthrough where the invading fluid reaches the downstream boundary of the field of view. A second kink followed by a plateau of the saturation is observed at the residual saturation $S = S_r$. (b–e) Examples of displacement patterns at residual and final saturation from experiments (b) and (c), respectively, and for simulations in (d) and (e).

saturation of the defending fluid decreases linearly with the injected volume of the invading fluid as long as the invading front is located completely within the field of view. Hence, the saturation S of the defending fluid, when plotted against the specific volume V/V^* of the injected fluid, decreases linearly with a slope -1, irrespective on the contact angle θ_a [see the plots in Fig. 3(a)]. However, after a certain volume V has been injected, the front of the invading fluid reaches the boundary of the field of view. This breakthrough occurs at the final saturation S_f where the saturation curve $S(V/V^*)$ departs from the linear decrease and starts to flatten before it finally levels off in a plateau, defining the residual saturation S_r of the defending fluid. In contrast to the residual saturations S_r, the final saturation S_f is governed solely by the arrangement of the posts within the field of view and is therefore insensitive to the particular downstream boundary conditions of our experiments or simulations. Thus, we will restrict our following discussion and in particular the comparison of the experimental and numerical results to the final saturation S_f of the defending fluid.

As expected from the evolution of the interface length, the final saturations S_f observed in our experiments and numerical simulations reveal two distinct wettability regimes [see Figs. 4(a) and 4(b)]. In the regime of small contact angles $\theta_a \lesssim 80°$ the displacement pattern is smooth and none or only a minute amount of the defending fluid remains in the field of view at the end of the experiment. However, in the regime of large contact angles $\theta_a \gtrsim 120°$, capillary fingers appear during the evolution of the displacement pattern that cause a certain fraction of the defending fluid to be retained in the array of posts at the end of the experiment. In both wetting regimes, the respective displacement patterns are insensitive with respect to the contact angle and independent of the displacement rate for sufficiently small interface velocities, as considered here.

The two observed regimes of final saturations at small and large contact angles and their crossover are still present in denser posts arrays with a higher area fraction of $\phi = 0.3$ [see Fig. 4(b)]. The experimentally determined final saturation S_f for the dense array with $\phi = 0.3$ appears to be systematically larger by a constant off-set ~ 0.15 when compared to the final saturations in a dilute post array with an area fraction $\phi = 0.15$ for the same contact angle θ_a.

B. Local advancing modes

The outstanding role of wettability in immiscible fluid displacement can be understood by considering the local invasion processes on the level of a few neighboring menisci. To characterize and to further describe the motion of the fluid interface in our experiments and simulations, we classify each interfacial instability leading to a local interfacial advance. Since we are working

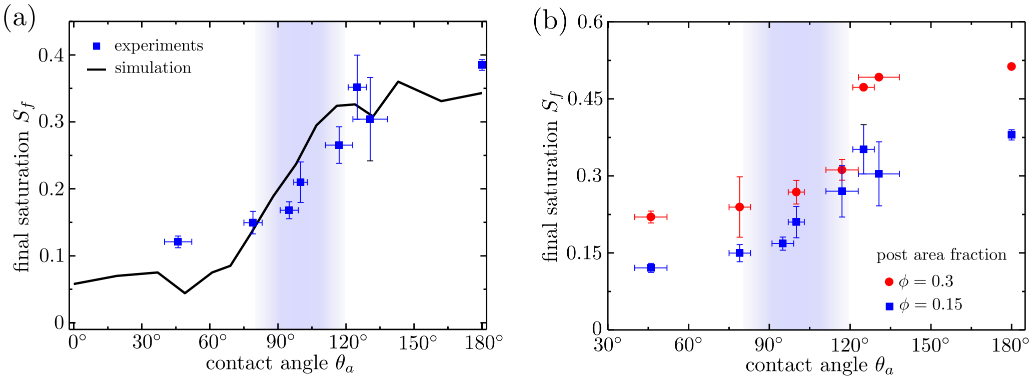

FIG. 4. (a) Final saturation S_f of the defending fluid as a function of the contact angle θ_a with respect to the invading fluid. Experimental data for post arrays with area fraction $\phi = 0.15$ (squares) in comparison to numerical data (solid line) for the same arrangement of posts. The shaded region emphasizes the extension of the crossover for contact angles $80^\circ \lesssim \theta_a \lesssim 120^\circ$, respectively. (b) Experimentally measured final saturation for $\phi = 0.15$ (squares) and $\phi = 0.3$ (circles) of the posts. Error bars on the abscissa (θ_a) and ordinate (S_f) represent the standard deviation of several measurements.

exclusively in the limit of quasistatic interfacial displacement and due to our temporal and spatial resolution, we can directly observe the four fundamental modes of local fluid advance, as initially introduced by Cieplak and Robbins [22,23]. The salient features of these interfacial instabilities are illustrated by overlays of snapshots of two meniscus configurations, one shortly before and a second during the instability in Fig. 5. Besides the burst and touch instability of a single meniscus, the invading interface can undergo two types of coalescence instabilities that involve two adjacent menisci.

In an ideal, pressure-controlled setup, a single meniscus spanning the gap between two posts becomes unstable and progresses whenever the meniscus contour exceeds a maximum in-plane curvature. In this case, any further advance of the three-phase contact line is accompanied by a decreasing curvature of the meniscus and thus a local decrease of the Laplace pressure. This decrease of the Laplace pressure drives a flow of the invading fluid until a new, stable interfacial configuration has been reached. Owing to the sudden fluid invasion after the breakthrough, this instability has been termed a burst. The typical evolution of a meniscus geometry before and during a burst instability is shown in Fig. 5(a).

Alternatively to the burst instability, the meniscus may touch a post that lies ahead of the front before the largest possible curvature is reached [see Fig. 5(b)]. Once the meniscus touches the post,

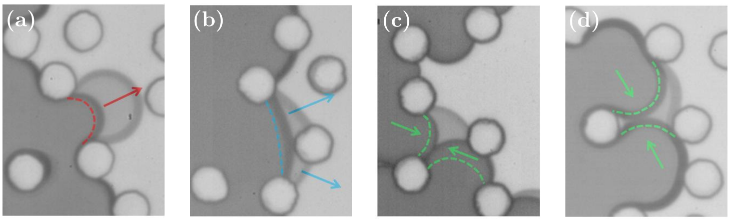

FIG. 5. Optical micrographs of meniscus instabilities in a Hele-Shaw cell decorated with an array of cylindrical posts for different wall wettability observed in our experiments: (a) burst, (b) touch, (c) coalescence where the three phase contact lines touch first, and (d) coalescence where the fluid-fluid interfaces touch first. Images of the meniscus configuration at the point of instability overlay the respective meniscus configurations after the instability (background). The dashed lines represent the position of a stable meniscus before instability.

it splits up into two menisci. Within a very short time the two newly formed menisci establish the material contact angle with the wall. In the course of this rearrangement, termed touch instability, the new menisci pull the invading fluid forward into the two empty gaps that are adjacent to the touched post. Similar to the burst instability, only a single meniscus is involved in a touch instability and the condition of a touch can be related to a maximum Laplace pressure of a single meniscus assigned to each individual gap. In contrast to the burst, this pressure maximum depends not only on the relative orientation of the meniscus with respect to the gap, but also on the relative position of the posts that are located ahead of the meniscus. The respective conditions for the occurrence of a touch or a burst instability are both independent of the state of the neighboring gaps, i.e., on whether these gaps are filled, empty, or partially wet by the invading fluid.

Besides undergoing a burst or touch instability, a meniscus can also collide with another meniscus and eventually coalesce to form a single meniscus. Coalescence events involve the menisci of two adjacent gaps and are thus fundamentally different from bursts and touches. As illustrated in Fig. 5(c), one can distinguish two types of coalescence events. In most cases the coalescence is triggered by a collision of the three-phase contact lines of the menisci that are located on the same post. In a few cases, particularly for high contact angles of the invading fluid, the two neighboring menisci touch and merge into a single meniscus, as illustrated in Fig. 5(d). Like for the burst and touch instabilities, the appearance of coalescence events is controlled by the contact angle with the sidewalls of the posts, the Laplace pressure, and the local post geometry.

C. Statistics of advancing modes

A quantitative analysis of the instabilities controlling the advancement of the invading fluid requires an unambiguous identification of the local front morphology. For low contact angles of the invading fluid, in particular, we need to find an unequivocal criterion to decide whether an observed meniscus shape is transient or represents a stable configuration. In practice, this task turns out to be difficult. Only stable meniscus configurations are consistent with the assumption of a quasistatic fluid invasion as demanded by the model of Cieplak and Robbins. Transient meniscus shapes that are far from a circular arc observed in experiments and simulations cannot be assigned to any of the advancing modes described in Sec. IV B. To reach a quantitative description, we adopt the rule that all meniscus shapes that exhibit local curvatures of both signs at the point of instability are counted as a transient shape.

Given that the topology of the invading interface at certain point in time is uniquely determined by the set of all pairs of posts that are connected by a meniscus, we can compute the number of menisci that have decayed due to touches N_t, bursts N_b, or coalescences N_c. A finite number of menisci N_a remains arrested until the end of the fluid invasion, i.e., until the front has reached its final stable configuration. Hence the total number of menisci observed during invasion is $N = N_t + N_b + N_c + N_a + N_*$, where N_* is the number of transient meniscus configurations that could not be assigned to one of the advancing modes discussed above.

Figure 6(a) summarizes the relative frequencies N_ξ/N that a meniscus progressed as a consequence of a certain advancing mode $\xi \in \{t,b,c\}$ and the fraction N_a/N of menisci that remained arrested for the series of contact angles θ_a of the invading fluid. In the range of small contact angles $\theta_a \lesssim 80^\circ$, exclusively touch and coalescence events are recorded. The relative frequency of arrested menisci at low contact angles is zero. At intermediate contact angles $80^\circ \lesssim \theta_a \lesssim 120^\circ$ the relative frequencies of touches and coalescences are continuously decreasing. In contrast, burst instabilities appear for the first time at a contact angle of approximately 80°. The relative frequency of bursts N_b/N is continuously increasing in the range of intermediate contact angles. Simultaneously with the increase of bursts, the relative frequency of menisci that remain arrested increases from 0 to around $N_a/N \approx 0.4$. In the range of large contact angles $\theta_a \gtrsim 120^\circ$ the relative frequency of arrested menisci plateaus at $N_a/N \approx 0.4$. Also the relative frequency of burst instabilities remains roughly constant at $N_b/N \approx 0.45$. The plot in Fig. 6(a) also demonstrates that the relative frequency for coalescences reaches a plateau at $N_c/N \approx 0.1$ for contact angles $\theta_a \gtrsim 120^\circ$, while touch instabilities

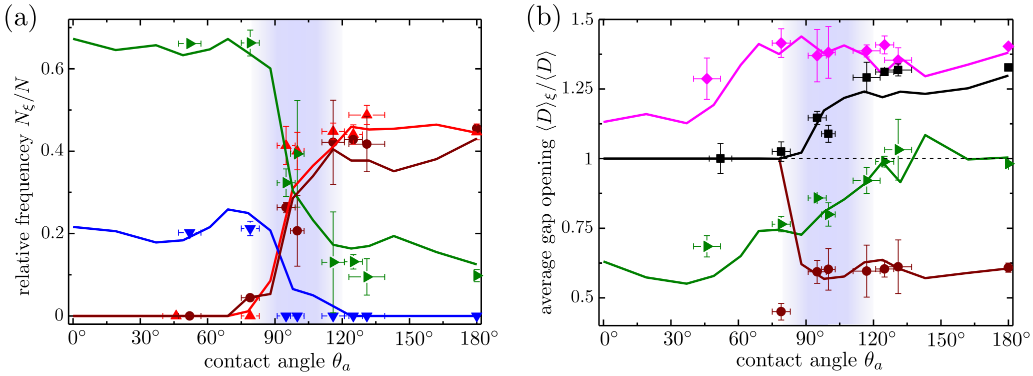

FIG. 6. (a) Relative frequency N_ξ/N of meniscus instabilities and arrested menisci as a function of the contact angle θ_a. (b) Average width $\langle D\rangle_\xi$ of gaps where the meniscus decayed by a certain instability ξ and where the meniscus remained arrested as a function of θ_a. The values $\langle D\rangle_\xi$ are normalized with the average gap size $\langle D\rangle$ of all pairs of cylindrical posts that were at least transiently connected by a meniscus. The experimental results are shown as symbols, i.e., coalescences (▶), touches (▼), bursts (▲), and arrested menisci (●). Corresponding results of simulation are shown as lines in the respective colors. To improve the significance of our statistic, bursts and touches are grouped to noncooperative instabilities (♦) in (b); all gaps that are filled at the end of an invasion are displayed as (■). Error bars on the abscissa (θ_a) represent the standard deviation of several measurements; error bars on the ordinate represent the respective statistical errors of the shown quantity. Shaded areas in (a) and (b) illustrate the crossover from the nonwetting to the wetting regime [see also Figs. 2(b) and 4].

completely vanish for $\theta_a \gtrsim 80^\circ$, simultaneously with the onset of bursts. At low contact angles, the coalescence starts from the three phase contact line [see Fig. 5(c)]. The complementary situation where the coalescence starts on the menisci occurs only for sufficiently high contact angles [see Fig. 5(d)]. Already at contact angles $\theta_a \gtrsim 80^\circ$, coalescences of the former type are fully suppressed because the meniscus does not protrude sufficiently far into the gap to touch a neighboring meniscus.

Figure 6(b) displays averages corresponding to the gap distance $\langle D\rangle_\xi$ for different advancing modes $\xi \in \{t,b,c\}$ or arrested menisci $\xi = a$. In the range of intermediate contact angles where N_t/N and N_b/N are small, the statistics of either the touch or burst events, respectively, display strong fluctuations [see Fig. 6(a)]. To improve the significance of averages $\langle D\rangle_\xi$ in Fig. 6(b), we thus grouped touches and bursts into the class of noncooperative instabilities, i.e., events involving a single meniscus, while coalescence events of two neighbored menisci are classified as cooperative instabilities. A comparison to Fig. 6(a) reveals how the frequencies of certain meniscus instabilities and of arrested menisci correlate with the gap opening $\langle D\rangle$. In the range of contact angles $\theta_a \lesssim 80^\circ$ the normalized average width of gaps that are filled at the end of an invasion remains constant at $\langle D\rangle_f = 1$ [see Fig. 6(b)]. In other words, all pairs of posts that were connected by a meniscus during the invasion for some time are filled with the invading fluid at the end of an experiment or simulation run. Coalescence events dominate the advancement for $\theta_a \lesssim 80^\circ$ and almost the entire defending fluid of the cell is displaced by the invading fluid. At higher contact angles $\theta_a \gtrsim 80^\circ$, i.e., above the onset of bursts, parts of defending fluid are trapped between the posts, which implies that a certain fraction of the gaps remains unfilled at the end of the invasion. Inspection of Fig. 6(b) reveals that the final average size of the gaps that are filled increases and plateaus at a value that is roughly $\langle D\rangle_f \approx 1.3\langle D\rangle$. However, considering only those gaps filled by noncooperative events, we even find a slightly larger average gap opening $\langle D\rangle_b \approx 1.4\langle D\rangle$. Defending fluid between posts with an average distance $\langle D\rangle_a \approx 0.6\langle D\rangle$ will never be displaced by the invading fluid. The smallest gaps in an array of posts are never filled and potentially block complete areas from invasion. Gaps involved in coalescence events display an average opening $\langle D\rangle_c/\langle D\rangle \lesssim 1$ in the range of contact angles $\theta_a \lesssim 120^\circ$ and $\langle D\rangle_c/\langle D\rangle \approx 1$ for large contact angles $\theta_a \gtrsim 120^\circ$.

V. DISCUSSION

Despite its immediate relevance in many industrial applications, a direct observation of the wettability-controlled crossover between stable and unstable immiscible displacement at low capillary numbers has been the subject of only a few experimental studies [2,11,48] and numerical models [21–27,49]. The majority of the latter works assumed triangular or square arrays of posts with randomized radii [22–26], in contrast to long-range disordered post arrangements considered in Ref. [49] and in the present study. The minimal surface-to-surface separation of neighboring posts in our Hele-Shaw cell is set to the diameter of the posts and is therefore larger than the typical distances of disks investigated in Refs. [21,22,26]. The relatively low area fraction of posts in the present work is necessary to reach the optical resolution that allows a further quantitative image analysis.

Small surface-to-surface separation and a regular geometry of the disk centers effectively limits the number of possible static meniscus configurations that need to be considered in a numerical implementation of models assuming quasistatic meniscus shapes [21,22,26]. Hence, a high area fraction of posts is advantageous in simulations that are based on a discrete representation of the invading interface. For large distances between the posts, however, only a small fraction out of the large set of potential quasistatic meniscus configurations of the interface can be represented in a network of predefined cells and gap openings. In this case, further *ad hoc* assumptions are required to predict the path of the invading fluid [49].

With the aim of following the morphological evolution of the front for identical post arrays in experiments and simulations, we solve the full fluid dynamics problem of the displacement process. In contrast to discrete network models, a full-scale simulation of the two-phase flow naturally respects all possible meniscus configurations that could be attained during invasion. Moreover, the meniscus shapes in a full fluid dynamics description may depart from the circular arc geometry assumed in the quasistatic model of Cieplak and Robbins. None of the aforementioned quasistatic models are able to reach conclusions about the transient meniscus shapes that occur immediately after a burst, touch, or coalescence instability.

Full-scale simulations of the progressing front account for the viscous pressure drop in the bulk fluids, a point that has been excluded from the original quasistatic model of Cieplak and Robbins. The recent model of Holtzman and Segre studied in Ref. [21] combines the quasistatic Laplace pressure-controlled geometrical approach of Cieplak and Robbins with a network model that includes pressure gradients of viscous flows. The relation between the local Laplace pressure of a meniscus and the filling degree of the corresponding throat [21] is still based on the assumption of circular arcs. *Ad hoc* assumptions are applied regarding the final meniscus states attained after an instability. As compared to network models, full-scale simulations of the fluid dynamics of immiscible displacement in Hele-Shaw cells are computationally demanding.

Although the modified capillary number Ca^* reaches up to $O(10)$ in our simulations of the invasion process, we never observe a Saffman-Taylor instability [50] and the subsequent formation of fingers. To suppress a Saffman-Taylor instability of the invading interface or, conversely, a front stabilization, we set the viscosity contrast between the defending and invading fluid to the marginally stable case $\mathsf{M} = 1$ in all simulation runs. Because the modified capillary number Ca^* is always smaller than unity in our displacement experiments, we can safely discard viscous fingering as the cause for ramified displacement patterns. Similarly, a stabilization of the invading front by viscous forces is also ruled out.

The morphology of the displacement pattern and the final saturation of the defending fluid in our experiments and simulations are obviously governed by the prevalence or absence of certain interfacial instabilities at the front. For invading fluids with a small contact angle $\theta_a \lesssim 80^\circ$, it is much more likely that a meniscus of the invading interface coalesces with a neighboring meniscus rather than decay in a burst or a touch instability. Accordingly, the tendency of the invading interface to remain in a straight configuration in the range of small contact angles $\theta_a \lesssim 80^\circ$ can be explained by the cooperativity of coalescence events. In this regime of small contact angles, the length of the interface fluctuates around a constant value (see Fig. 2).

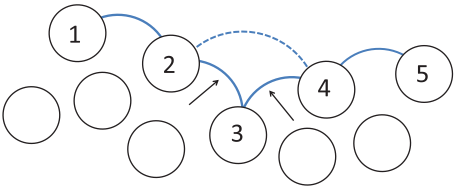

FIG. 7. Sketch of a meniscus configuration. The interface between posts 2, 3, and 4 forms a local recess where the corresponding menisci are oriented towards each other. Here a coalescence event that smoothens the invading interface (indicated by the dashed line) is strongly favored.

A comparison of the statistics of meniscus advancing modes in Fig. 6(a), the growth rate of the interface length in Fig. 2(b), and the final saturations in Fig. 4 reveals that the extensions of the regime of touch and coalescence events at low contact angles, as well as the regime of bursts at high contact angles, coincide with the respective regimes of low and high final saturation. For the experimental data corresponding to contact angles of $\theta_a = 95^\circ$ and $\theta_a = 100^\circ$ we observe a systematic shift of the experimental data compared to the numerical data towards a higher contact angle in both Figs. 2(b) and 4. In the same range of contact angles one can also notice a slight deviation in the statistics of interfacial instabilities (see Fig. 6). However, except for contact angles in the range of this crossover, we find excellent quantitative agreement of both growth rates of interfacial length and final saturations between the respective results of our experiments and numerical simulations. This match supports our hypothesis that only the advancing contact angle has a noticeable influence on the dynamics of fluid invasion. Advancing and receding contact angles are identical in our simulation, which implies that a qualitative difference from the displacement process could only be expected if some parts of the interface in our experiments were also retracting into the direction of the invading fluid.

The coalescence of two neighboring menisci into a single meniscus is strongly favored whenever the coalescing menisci are oriented toward each other (see Fig. 7). As a consequence of this bias, any local recess of the interface that may have formed due to other capillary instabilities such as bursts and touches is quickly erased as the interface progresses. Similarly, coalescence instabilities are unlikely to occur in configurations where two menisci are oriented away from each other like in a local protrusion of the invading fluid. This particular dependence of the coalescence events on the relative orientation of neighboring menisci readily explains the tendency of the interface to remain in an overall straight configuration when coalescence dominates. Observing the invasion process in a coarse-grained picture, i.e., on a length scale much larger than the scale of the posts, the cooperative invasion modes suppress the buildup of large excursions of the interface similar to a global interfacial tension [51]. In contrast to the true microscopic interfacial tension of the menisci, this effective tension is inherently linked to the invasion dynamics. Despite this dynamically generated stiffness of the moving interface, we can expect that the noise caused by subsequent pinning and depinning events will, to a certain extent, progressively roughen the invading interface [33,34,52].

In the opposite limit of large contact angles $\theta_a \gtrsim 120^\circ$ of the invading fluid, the interface remains pinned at the posts in the majority of cases. Instead of coalescences, the dominant modes of interfacial advance observed in our experiments and simulations are burst instabilities. Because burst events are uncorrelated and randomly distributed over the invading interface in a disordered post array, the dynamics of a slow fluid displacement can be described by an invasion percolation model [53,54]. As expected for an invasion percolation process, we observe a strong fingering of the interface and thus an increase of its length with the injected volume (cf. the plots of interface length against the injected pore volume in Fig. 2). The linear growth of the interfacial length in the regime of contact angles $\theta_a \gtrsim 120^\circ$ is consistent with the formation of a ramified displacement pattern [53,54]. Percolation theory predicts that the surface of the invading clusters, i.e., the number of dangling bonds, grows linearly with the number of occupied bonds for asymptotically large clusters [55,56]. The slight sublinear trend observed in our numerical simulations hints at a finite-size effect related to the lateral confinement.

In accord with the statistics of the local advancing modes of the interface shown in Fig. 6(a), the average gap width $\langle D\rangle_f$ of filled gaps for $\theta_a \gtrsim 120^\circ$ is significantly larger than the average gap width $\langle D\rangle$ over all advancing modes including arrested menisci and transient configurations. This finding can be easily explained from the dominance of burst instabilities at high contact angles. Bursts occur at the gap with the lowest critical Laplace pressure. Since the contact angle is the same on all posts, the lowest critical pressure is found at the gap with the largest opening. The burst criterion explains the strong correlation of progressing menisci and large gaps. This correlation can be observed only if the meniscus does not undergo a different type of instability before the burst criterion is reached.

A preference of coalescences to occur at small gap openings in the range of large contact angles $\theta_a \leqslant 120^\circ$, as revealed by Fig. 6(b), is rather a consequence of the competition with burst instabilities that have a clear preference to occur at gaps with openings above average. Coalescence events are favored by small contact angles but, in principle, can be observed over the full range of contact angles. Our experiments and fluid dynamics simulations indicate that the coalescence of the three-phase contact line of the menisci in fact plays "…the crucial role in changing the growth pattern as θ_a is varied" as already suggested by Cieplak and Robbins in Ref. [23].

Judging from the final saturation S_f as a function of the contact angle θ_a shown in Fig. 4, the crossover between cooperative and noncooperative modes of interfacial advance is unchanged between area fractions $\phi = 0.15$ and 0.3 of the posts. This finding is at variance with data reported for the quasistatic model in Refs. [22,23], showing that the transition between a smooth and a ramified invading interface occurs at smaller contact angles in disk arrays with higher area fractions. Given the finite height of the Hele-Shaw cell, the particular three-dimensional geometry of the meniscus can easily cause systematic deviations from the effectively two-dimensional model, particularly for high area fractions and aspect ratios of the posts. Enlarged final saturations observed in arrays of denser posts could also be a particular consequence of the pore-scale fluid dynamics leading, e.g., to a number of smaller fluid pockets of the defending phase even at low contact angles $\theta_a \lesssim 80^\circ$ where coalescence is the dominant mode of interfacial advance.

VI. CONCLUSION AND OUTLOOK

The present experimental and numerical results demonstrate that wettability is a key parameter to understand the displacement of a defending fluid by an invading immiscible fluid from a quasi-two-dimensional Hele-Shaw cell with cylindrical posts. Fluid displacement patterns recorded in experiments display excellent agreement with those found in fluid dynamics simulation of the invasion process for identical positions of the posts. Supported by this perfect match, we propose two regimes of displacement pattern in terms of wettability. In each of the two regimes, the final saturation of the defending fluid is widely independent on the contact angle θ_a. In the regime of wetting invading fluids $\theta_a \lesssim 80^\circ$, the interface remains smooth while the defending fluid is displaced almost completely from the cell. In the poorly wettable regime $\theta_a \gtrsim 120^\circ$, the interface evolves into a ramified geometry and a significant amount of defending fluid is trapped between the posts and remains in the cell. The global dynamics of the displacement and with it the final amount of the defending fluid can be understood in terms of local interfacial instabilities.

Both observed displacement patterns can be related to the dominance of either cooperative or noncooperative meniscus instabilities in the course of front progression. A statistical analysis of the appearing instabilities clearly shows that the prevalence of the cooperative coalescences at low contact angles of the invading fluid (imbibition) leads to a stable interface advance and low residual saturations. For high contact angles of the invading fluid, we observe that noncooperative burst instabilities dominate the interface advance and, consequently, capillary fingering and larger residual saturations. In accord with the model of Cieplak and Robbins [22,23], we observe that already small changes of the advancing contact angle in the crossover between the two regimes can lead to large changes in the displacement patterns. The results presented in this work provide clear evidence that the wettability-controlled transition between a smooth interfacial advance and capillary fingering is not restricted to post arrays with positional order, as originally considered in Refs. [22,23].

So far, a noticeable roughening of the invading interface in the regime of stable advance could be observed neither in our experiments nor in the corresponding full-scale fluid dynamics simulations. Hence, we expect that the influence of the quenched disorder in the Hele-Shaw cell introduced by the posts will become apparent only in systems with larger extensions. It will be particularly interesting to quantify the buildup of interfacial roughness in the narrow crossover between the stable interfacial advance and capillary fingering.

The competition between cooperative and noncooperative pore invasion will affect, in principle, slow immiscible fluid displacement in any two- and three-dimensional porous matrices. One of the important questions arising in this context is whether the wettability-controlled crossover between stable interfacial advance and capillary fingering applies also to real three-dimensional porous media. Even for the most simple three-dimensional experimental system, a disordered bed of uniformly wettable spherical beads, it is already a formidable task to determine the spectrum of possible local interfacial configurations for a given Laplace pressure and contact angle. Compared to the effectively two-dimensional Hele-Shaw cell, the catalog of interfacial instabilities that can lead to a local fluid advance in dense beds of spherical beads is considerably more complex and further simplifications are necessary to formulate a tractable model that is able to provide quantitative predictions.

ACKNOWLEDGMENTS

The author would like to thank Jean-Christophe Baret, Benoit Semin, Julie Murison, Anne Muggeridge, Bilal Rashid, and Jean-Babtiste Fleury for fruitful discussions. Generous support was granted by the ExploRe program of BP plc.

APPENDIX A: MICROFLUIDIC DEVICE AND FLUID PROPERTIES

To achieve an initial straight interface of the invading fluid into the structured area, the main inlet channel is branched twice injecting the invading fluid via four inlets into the post array (see Fig. 8). A subsequent gap of 100 μm after the branched inlet channels allows the four interfaces to merge

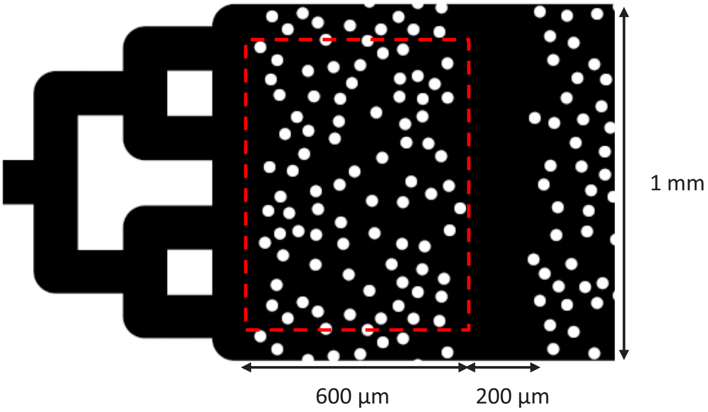

FIG. 8. Sketch of a microfluidic device with an area fraction of posts $\phi = 0.15$. The total width of the channel is 1000 μm. The dashed rectangle indicates the field of view in our experiments with a width of 800 μm and an extension in channel direction of 600 μm. The average surface-to-surface separation between two neighboring posts is $\langle D\rangle = (43 \pm 22)$ μm.

TABLE I. Fluid density and viscosity.

Fluid	Density ($\mathrm{g/cm^3}$)	Viscosity (mPa s)
air	1.18	0.017
water	0.99	0.9
dodecane	0.75	1.5
FC-75, FC-70	1.76,1.94	1.4,27.2
silicon oil AK10, AK50	0.93,0.96	9.3,48
silicon oil AK100, AK500	0.96,0.97	96,485

before entering the post array in the Hele-Shaw cell. The region of the post array that is captured in the experiments is indicated by the dashed box in Fig. 8, which has a width of 800 μm and extends about 600 μm in the channel direction. A gap of 200 μm is inserted behind the array of posts to guarantee defined end conditions.

To systematically vary the wettability different combinations of fluids, including air, water, dodecane (Merck), fluorinated oils (3M), and silicon oils (Wacker Chemie), as invading and defending fluids were used in combinations with the two device materials NOA 83H and NOA 61 (Norland Optical Adhesives). In one case we added 0.0037 wt.% of the surfactant sodium dodecylbenzenesulfonate (SDBS) (Sigma Aldrich) to the water to fine-tune the wettability. To optically distinguish the invading from the defending fluid, we added 3 wt.% of the dye erioglaucine (Sigma Aldrich) to water and 0.6 wt.% of the dye Oil Red O (Sigma Aldrich) to dodecane. The applied combinations of fluids and the relevant physical properties, as given by the respective manufacturers, are summarized in Tables I and II.

APPENDIX B: MODIFIED CAPILLARY NUMBER

For viscosity ratios $\mathsf{M} > 1$, an estimate can be obtained from a comparison of two pressure scales. In the case of a nonwetting invading fluid, the width of the front ξ_f can be related to the distribution of threshold values $P^{\max}$ of the Laplace pressures that a meniscus has to exceed to invade the space downstream of the gap. The relevant contribution to the Laplace pressure $P^{\max}$ for this instability is related only to the in-plane curvature of the meniscus. Given the surface-to-surface distances D of

TABLE II. Interfacial tension γ for the applied fluid-liquid combination and their advancing (θ_a) and receding (θ_r) contact angles on the respective NOA surfaces.

Injected fluid	Defending fluid	Device material	θ_a (deg)	θ_r (deg)	γ (mN/m)
dodecane	air	NOA 83H	<20	≈ 0	(25 ± 1)
water[a]	air	NOA 61	(46 ± 6)	<20	(35 ± 1)
water[b]	air	NOA 83H	(79 ± 4)	<20	(70 ± 1)
water[b]	FC-75	NOA 83H	(95 ± 4)	<20	(28 ± 1)
water[b]	FC-70	NOA 83H	(100 ± 3)	<20	(35 ± 2)
water[b]	silicon oil	NOA 83H	(117 ± 6)	<20	(28 ± 2)
water[b]	dodecane	NOA 83H	(125 ± 4)	<20	(26 ± 1)
dodecane[c]	water	NOA 83H	(131 ± 6)	<20	(48 ± 1)
air	dodecane	NOA 83H	≈ 180	>160	(25 ± 1)

[a] Water with 3 wt.% erioglaucine and 0.0037 wt.% SDBS.

[b] Water with 3 wt.% erioglaucine.

[c] Dodecane with 0.6 wt.% Oil Red O.

a pair of neighboring posts, we have $P^{\max} \approx -2\gamma \cos\theta_a/D$. The viscous pressure drop P^{visc} across the front must be just as large as to fill the large gaps at the tip of the front and the small gaps in the back of the front at the same time. Neglecting the increase of viscous pressure drop caused by the cylindrical post (which is ideally the case for $H \ll D$), we estimate $P^{\text{visc}} \approx \mu_i U W \xi_f/\langle D\rangle H^2$ for the "bare" Hele-Shaw geometry without posts, where we use an upper bound $WU/\langle D\rangle$ on the local flow velocity at the invading front.

Effects caused by the viscous pressure drop are irrelevant whenever the longitudinal dimensions of the Hele-Shaw cell L are much smaller than ξ_f. Employing the width of the distribution ΔD of gap separations D to estimate the difference between the largest and the smallest value of the threshold pressure $P^{\max}$, we finally arrive at the condition

$$\text{Ca}^* \equiv \frac{6\mu_i\langle D\rangle LWU}{\gamma|\cos\theta_a|\Delta D H^2} \ll 1 \tag{B1}$$

to operate in the regime where the final pattern of the displaced fluid is independent of the injection rate of the invading fluid.

In the quasi-two-dimensional flow of the simulations, the hydraulic resistance of an array of cylinders [57] gives rise to the modified capillary number

$$\text{Ca}^* = \frac{4\mu_i U\langle D\rangle LW}{f\left(\frac{\langle B\rangle}{2R}\right)\gamma|\cos\theta_a|\Delta D\langle B\rangle^2}, \tag{B2}$$

where $\langle B\rangle = \langle D\rangle + 2R$ is the average center-to-center distance of two posts and the expression $f(x)$ in the denominator of (B2) takes on the form

$$f(x) = \ln x - \frac{1}{2}\frac{x^4-1}{x^4+1}. \tag{B3}$$

For the standard post arrangement used in experiments and simulations with area fraction of $\phi = 0.15$, we have $\Delta D \approx \langle D\rangle/2$, where $\langle D\rangle$ is the mean surface-to-surface separation between two neighboring posts. Since $W \approx 30H$ and $L \approx 20H$ we find $\text{Ca}^* \approx 9 \times 10^3\text{Ca}$ for the experiments and $\text{Ca}^* \approx 2.9 \times 10^3\text{Ca}$ for the corresponding numerical simulations. In both cases, we assume $|\cos\theta_a| \approx 0.8$ as a lower bound, since capillary fingering is not observed for contact angles below $\theta_a \lesssim 120^\circ$.

---

[1] Z. H. Wang, C. Y. Wang, and K. S. Chen, Two-phase flow and transport in the air cathode of proton exchange membrane fuel cells, J. Power Sources **94**, 40 (2001).

[2] O. Chapuis, M. Prat, M. Quintard, E. Chane-Kane, O. Guillot, and N. Mayer, Two-phase flow and evaporation in model fibrous media: Application to the gas diffusion layer of PEM fuel cells, J. Power Sources **178**, 258 (2008).

[3] R. Anderson, L. Zhang, Y. Ding, M. Blanco, X. Bi, and D. P. Wilkinson, A critical review of two-phase flow in gas flow channels of proton exchange membrane fuel cells, J. Power Sources **195**, 4531 (2010).

[4] J. Bear, *Dynamics of Fluids in Porous Media* (Elsevier, New York, 1972).

[5] N. R. Morrow, Wettability and its effect on oil recovery, J. Pet. Technol. **42**, 1476 (1990).

[6] M. Sahimi, *Flow and Transport in Porous Media and Fractured Rock* (Wiley-VCH, Weinheim, 2011).

[7] A. Muggeridge, A. Cockin, K. Webb, H. Frampton, I. Collins, T. Moulds, and P. Salino, Recovery rates, enhanced oil recovery and technological limits, Philos. Trans. R. Soc. London A **372**, 20120320 (2014).

[8] A. Krummel, S. Datta, S. Münster, and D. Weitz, Visualizing multiphase flow and trapped fluid configurations in a model three-dimensional porous medium, AIChE J. **59**, 1022 (2013).

[9] S. S. Datta, T. S. Ramakrishnan, and D. A. Weitz, Mobilization of a trapped non-wetting fluid from a three-dimensional porous medium, Phys. Fluids **26**, 022002 (2014).

[10] J. Murison, B. Semin, J.-C. Baret, S. Herminghaus, M. Schröter, and M. Brinkmann, Wetting heterogeneities in porous media control flow dissipation, Phys. Rev. Appl. **2**, 034002 (2014).

[11] M. Trojer, M. L. Szulczewski, and R. Juanes, Stabilizing fluid-fluid displacements in porous media through wettability alteration, Phys. Rev. Appl. **3**, 054008 (2015).

[12] G.-Q. Tang and A. R. Kovscek, High resolution imaging of unstable, forced imbibition in Berea Sandstone, Transp. Porous Media **86**, 617 (2011).

[13] S. Iglauer, M. A. Fernø, P. Shearing, and M. J. Blunt, Comparison of residual oil cluster size distribution, morphology and saturation in oil-wet and water-wet sandstone, J. Colloid Interface Sci. **375**, 187 (2012).

[14] L. Leu, S. Berg, F. Enzmann, R. T. Armstrong, and M. Kersten, Fast x-ray micro-tomography of multiphase flow in Berea Sandstone: A sensitivity study on image processing, Transp. Porous Media **105**, 451 (2014).

[15] R. Lenormand, E. Touboul, and C. Zarcone, Numerical models and experiments on immiscible displacements in porous media, J. Fluid Mech. **189**, 165 (1988).

[16] C. Zhang, M. Oostrom, T. W. Wietsma, J. W. Grate, and M. G. Warner, Influence of viscous and capillary forces on immiscible fluid displacement: Pore-scale experimental study in a water-wet micromodel demonstrating viscous and capillary fingering, Energy Fuels **25**, 3493 (2011).

[17] C. Cottin, H. Bodiguel, and A. Colin, Influence of wetting conditions on drainage in porous media: A microfluidic study, Phys. Rev. E **84**, 026311 (2011).

[18] H. Lee, S. G. Lee, and P. S. Doyle, Photopatterned oil-reservoir micromodels with tailored wetting properties, Lab Chip **15**, 3047 (2015).

[19] M. J. Blunt, Flow in porous media–Pore-network models and multiphase flow, Curr. Opin. Colloid Interface Sci. **6**, 197 (2001).

[20] D. Wildenschild and A. P. Sheppard, X-ray imaging and analysis techniques for quantifying pore-scale structure and processes in subsurface porous medium systems, Adv. Water Resour. **51**, 217 (2013).

[21] R. Holtzman and E. Segre, Wettability Stabilizes Fluid Invasion into Porous Media Via Nonlocal, Cooperative Pore Filling, Phys. Rev. Lett. **115**, 164501 (2015).

[22] M. Cieplak and M. O. Robbins, Dynamical Transition in Quasistatic Fluid Invasion in Porous Media, Phys. Rev. Lett. **60**, 2042 (1988).

[23] M. Cieplak and M. O. Robbins, Influence of contact angle on quasistatic fluid invasion of porous media, Phys. Rev. B **41**, 11508 (1990).

[24] N. Martys, M. Cieplak, and M. O. Robbins, Critical Phenomena in Fluid Invasion of Porous Media, Phys. Rev. Lett. **66**, 1058 (1991).

[25] B. Koiller, H. Ji, and M. O. Robbins, Fluid wetting properties and the invasion of square networks, Phys. Rev. B **45**, 7762 (1992).

[26] H. Chraïbi, M. Prat, and O. Chapuis, Influence of contact angle on slow evaporation in two-dimensional porous media, Phys. Rev. E **79**, 026313 (2009).

[27] H. A. Akhlaghi Amiri and A. A. Hamouda, Pore-scale modeling of non-isothermal two phase flow in 2D porous media: Influences of viscosity, capillarity, wettability and heterogeneity, Int. J. Multiphase Flow **61**, 14 (2014).

[28] R. T. Armstrong and S. Berg, Interfacial velocities and capillary pressure gradients during Haines jumps, Phys. Rev. E **88**, 043010 (2013).

[29] S. Berg, H. Ott, S. A. Klapp, A. Schwing, R. Neiteler, N. Brussee, A. Makurat, L. Leu, F. Enzmann, J.-O. Schwarz, M. Kersten, S. Irvine, and M. Stampanoni, Real-time 3D imaging of Haines jumps in porous media flow, Proc. Natl. Acad. Sci. USA **110**, 3755 (2013).

[30] F. Moebius and D. Or, Interfacial jumps and pressure bursts during fluid displacement in interacting irregular capillaries, J. Colloid Interface Sci. **377**, 406 (2012).

[31] F. Moebius and D. Or, Inertial forces affect fluid front displacement dynamics in a pore-throat network model, Phys. Rev. E **90**, 023019 (2014).

[32] R. Lenormand, C. Zarcone, and A. Sarr, Mechanisms of the displacement of one fluid by another in a network of capillary ducts, J. Fluid Mech. **135**, 337 (1983).

[33] A. Herńandez-Machado, J. Soriano, A. M. Lacasta, M. A. Rodriguez, L. Ramirez-Piscina, and J. Ortín, Interface roughening in Hele-Shaw flows with quenched disorder: Experimental and theoretical results, Europhys. Lett. **55**, 194 (2001).

[34] M. Pradas, J. M. López, and A. Hernández-Machado, Avalanche dynamics in fluid imbibition near the depinning transition, Phys. Rev. E **80**, 050101 (2009).
[35] R. Lenormand, Liquids in porous media, J. Phys.: Condens. Matter **2**, SA79 (1990).
[36] Y. Xia and G. Whitesides, Soft lithography, Annu. Rev. Mater. Sci. **28**, 153 (1998).
[37] P. Concus and R. Finn, On the behavior of a capillary surface in a wedge, Proc. Natl. Acad. Sci. USA **63**, 292 (1969).
[38] Y. Inoue, Y. Chen, and H. Ohashi, A mesoscopic simulation model for immiscible multiphase fluids, J. Comput. Phys. **201**, 191 (2004).
[39] Y. Inoue, S. Takagi, and Y. Matsumoto, A mesoscopic simulation study of distributions of droplets in a bifurcating channel, Comput. Fluids **35**, 971 (2006).
[40] T. Hiller, M. S. de La Lama, and M. Brinkmann, Stochastic rotation dynamics simulations of wetting multi-phase flows, J. Comput. Phys. **315**, 554 (2016).
[41] A. Malevanets and R. Kapral, Mesoscopic model for solvent dynamics, J. Chem. Phys. **110**, 8605 (1999).
[42] A. Malevanets and R. Kapral, Solute molecular dynamics in a mesoscale solvent, J. Chem. Phys. **112**, 7260 (2000).
[43] R. Kapral, Multiparticle collision dynamics: Simulation of complex systems on mesoscales, Adv. Chem. Phys. **140**, 89 (2008).
[44] G. Gompper, T. Ihle, D. Kroll, and R. G. Winkler, *Advanced Computer Simulation Approaches for Soft Matter Sciences III* (Springer, Berlin, 2009).
[45] P. J. Hoogerbrugge and J. M. V. A. Koelman, Simulating microscopic hydrodynamic phenomena with dissipative particle dynamics, Europhys. Lett. **19**, 155 (1992).
[46] P. Español and P. Warren, Statistical mechanics of dissipative particle dynamics, Europhys. Lett. **30**, 191 (1995).
[47] J. M. Haile, *Molecular Dynamics Simulation* (Wiley, New York, 1992).
[48] W. G. Anderson, Wettability literature survey-Part 6: The effects of wettability on waterflooding, J. Pet. Technol. **39**, 1605 (1987).
[49] S. Motealleh, M. Ashouripashaki, D. DiCarlo, and S. Bryant, Mechanisms of capillary-controlled immiscible fluid flow in fractionally wet porous media, Vadose Zone J. **9**, 610 (2010).
[50] P. G. Saffman and G. Taylor, The penetration of a fluid into a porous medium or Hele-Shaw cell containing a more viscous liquid, Proc. R. Soc. London Ser. A **245**, 312 (1958).
[51] R. Rangel and S. Rojas, Montecarlo DLA-type simulations of wetting effects in fluid displacement in porous media, Comput. Geosci. **13**, 215 (2009).
[52] M. Alava, M. Dubé, and M. Rost, Imbibition in disordered media, Adv. Phys. **53**, 83 (2004).
[53] D. Wilkinson and J. F. Willemsen, Invasion percolation: A new form of percolation theory, J. Phys. A: Math. Gen. **16**, 3365 (1983).
[54] M. M. Dias and D. Wilkinson, Percolation with trapping, J. Phys. A: Math. Gen. **19**, 3131 (1986).
[55] C. Domb, T. Schneider, and E. Stoll, Cluster shapes in lattice gases and percolation, J. Phys. A: Math. Gen. **8**, L90 (1975).
[56] D. Stauffer and A. Aharony, *Introduction To Percolation Theory* (CRC, Boca Raton, 1994).
[57] J. Happel, Viscous flow relative to arrays of cylinders, AIChE J. **5**, 174 (1959).